Set-up and test of the slow control and calibration of the photomultiplier of an apparatus to measure the reflectivity of teflon in LXe at VUV wavelengths

Florian Sprenger

2013/08/30

Contents

1 Dark Matter

The biggest human question "Where do we come from? Where are we going?" is directly connected to the question "What does the universe look like?". While astronomy observations gave us the first attempts at understanding the universe, at the scales of galaxies, particle physics now attempts at discovering its matter element content.

1.1 Pie of the universe

Nowadays our understanding of the content of the universe is that it is divided in three components: Baryonic matter, dark matter and dark energy. Baryonic matter is the matter which interacts with photons and we can see. Dark matter is the part of matter that does not interact with photons by the electromagnetic force. That is the reason why it is called "dark". The final and largest component of the universe, dark energy, was predicted by Einstein [1] through a parameter called the cosmological constant which explains the expansion of the universe [2]. However, except for its quantity, we know nothing about this dark energy.
The proportion of these components are given in the "Pie of the Universe" (fig. 1.1).

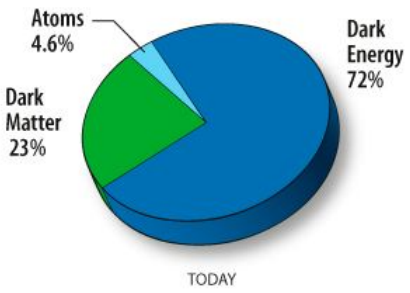

Figure 1.1: Content of the universe as a pie chart. Credits: NASA / WMAP Science Team

1.2 Evidence for Dark Matter

As shown in fig. 1.1, 23 % of the universe is Dark Matter (DM). The first prediction of DM was by Zwicky in 1933 [3]. By now there are several different evidences for DM. The three most important proofs are galactic rotation curves, gravitational lensing and the cosmic microwave background.

1.2.1 Galactic Rotation Curves

This proof of DM is based on the rotational velocity of the arms of spiral galaxies out of Newtonian mechanics. According to Newtonian mechanics that the attraction of the gravitation F_G compensates the centripetal force F_c the velocity v should go as

$$\begin{aligned} F_c &= F_G \\ \frac{mv^2(r)}{r} &= G\frac{M(r)\cdot m}{r^2} \\ v^2(r) &= \frac{GM(r)}{r} \\ v(r) &= \sqrt{GM(r)/r}. \end{aligned} \tag{1.1}$$

Here v is the velocity of an object with the mass m in an arm of a spiral galaxy, M is the mass of the hole galaxy and G is the constant of gravitation. But the rotational velocitiy in spiral galaxies is for bigger r nearly constant. This is shown in fig. 1.2.

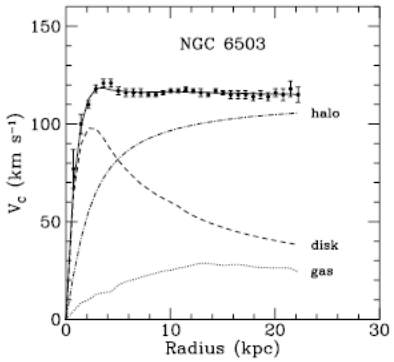

Figure 1.2: Measured rotation curve along with the mass contributions as a function of radius, for the visible component (dashed), the gas component (dotted), and the DM halo (dash dotted). Figure from Bergeman et al. (1991)

This effect can be explained by a rising DM halo with

$$M(r) \propto r \tag{1.2}$$

for the radius r. Because the Milky Way is a typical spiral galaxy these measurements of galactic rotation curves are very useful to evaluate the local DM density in our galaxy which is $\rho_{\mathrm{DM}} = 1.25^{+0.30}_{-0.34}$ GeV/cm^3 [4].

1.2.2 Gravitational Lensing

Gravitational lensing is a phenomenon which was predicted by Einstein's general theory of relativity. It develops when a massive object is between the observer and a far away obejct. In this case the radiation of the far away object is bent by the massive object which acts like a lens or multiple pictures of the observed object are visible (strong gravitational lensing). In case of weak gravitational lensing it is not directly observable that the radiation is bent by a far away object. Therefore a statistical measurement of multiple objects behind the lens is needed. By measuring the angle θ of the gravitational lensing, the mass of the massive object M can be computated:

$$M = \frac{\theta r c^2}{4G}. \tag{1.3}$$

In this equation which comes out of the general theory of reletavity [5] G is the universal constant of gravitiy, c the speed of light in vacuum and r the distance between the observer and the massive object. The distance r can be taken by the redshift z of the Bullet Cluster according to Hubble's law

$$r = \frac{c}{H_0} z \tag{1.4}$$

with the Hubble constant H_0 and the speed of light c [6].
The effect of weak lensing is observable in the Bullet Cluster (1E 0657-558) that is shown in fig. 1.3. The Bullet Cluster is a collision of two galaxies. On this picture the yellow regions are hot plasma. The blue area around it are the stars of the galaxies. Because the plasma is slowed down by the collision it has a higher density than the stars which pass through each other without slowing down. Therefore the main mass distribution should be where the plasma regions are. This is not the case. The green lines are the gravitational potential calculated by the effect of weak lensing of the Bullet Cluster. Out of this potential the mass distribution has to be outside of the centre of the Bullet Cluster.

1.2.3 Cosmic Microwave Background

The cosmic microwave background (CMB) was discovered in 1965 ([7], [8]). It is the measurement of intreminable background radiation that pervades the universe, therefore CMB is a very important arch for the big bang theory. In general CMB is isotropic over the whole sky, but in more detail there are tiny temperature fluctuations in it (fig. 1.4). These fluctuations are caused by primordial fluctuations in the mass density. The temperature fluctions of the

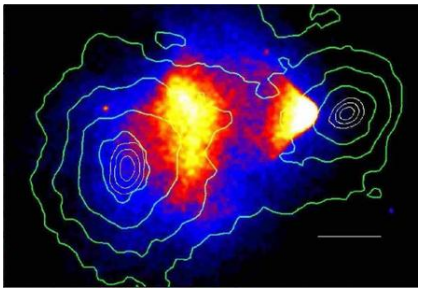

Figure 1.3: Distribution of hot baryonic plasma (yellow), the gravitational potential (green lines) and out of these two components the estimated DM halo. Credits: Chandra x-ray telescope

CMB were measured for nine years by the Wilkinson Microwave Anisotropy Probe (WMAP). Out of this measurement the physical cold dark matter density $\Omega_c h^2 = 26$ % is extracted [9].

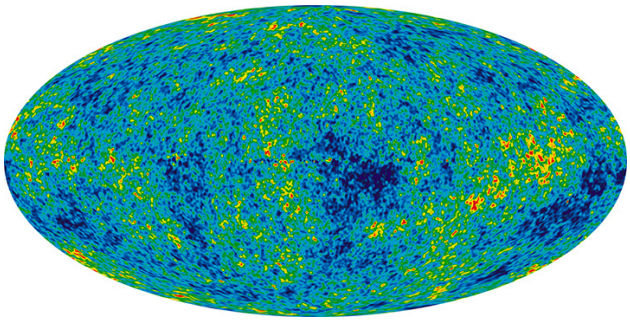

Figure 1.4: Map of the temperature of the CMB. Credits: NASA / WMAP Science Team

1.3 DM Candidates

Because DM particles don't interact with photons the electromagnetic interaction is suppressed for DM candidates. They have to be non-baryonic and can just interact with each other by forces that are weaker than the weak force (e.g. gravitation). The only particles known by now with these characteristics are neutrinos. But the number of them is too small to be responsible for the largest part of DM [10]. So there has to be different particles that are not known by now. These particles are called weakly interacting massive particles (WIMPs) beacause they only interact weakly with baryonic matter. In the early universe WIMPs were produced and annihilated into baryonic particles at equal rates. With expanding and cooling down of the universe

the WIMP production stopped and the WIMP density decreased until the annihilation interactions were not likely anymore. So the growing of universe left a WIMP density that accounts for the DM mass.

1.4 Supersymmetry

The current theoretical model for particle phyiscs is the standard model (SM). This describes the particles and the forces between them. But the SM cannot solve every question yet. Therefore supersymmetry (SUSY) is formed to answer open questions of the standard model. In SUSY every boson has a supersymmetric partner which is a fermion and the super-partner of every fermion is a boson (fig. 1.5). Thus the number of particles of the SM is doubled [11].
The model of supersymmetry is attractive because it describes also gravitational forces in contrast to the standard model. It solves open questions like the hierarchy problem or the non-zero rest mass of the neutrino [12]. Finally it also answers the question of the DM particle. The lightest supersymmetric particle (neutralino) is a good theoretical candidate for a WIMP.

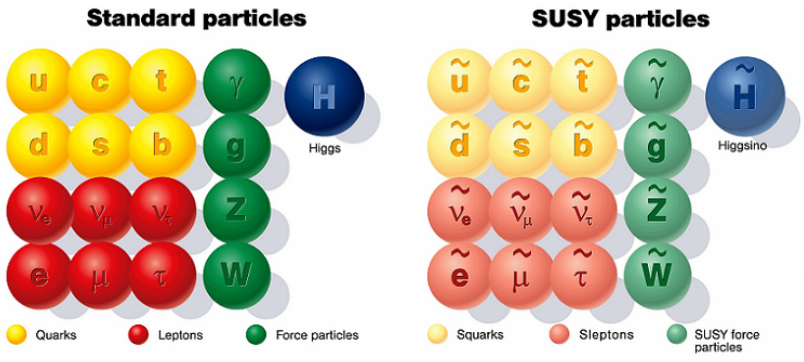

Figure 1.5: Particles of the standard model (left) with their supersymmetric particles (right). Credits: DESY

1.5 Experiments

If this supersymmetric particle exists, then it can be found through three different ways. The first way is the observation of cosmic rays coming from an annihilation of two WIMPs like it happened often in the early universe. The second way is a collider production. This is the invertion of the annihilating process of WIMPs. This means in the environment of high energy DM

particle can originate. This is motivated by the mass-energy equivalence

$$E = mc^2 \tag{1.5}$$

with E for the energy, m for the rest mass and c for the speed of light in vacuum [13]. The third one is a direct observation of the recoil between a WIMP and a nuclues. These three detecting ways are shown in fig. 1.6.

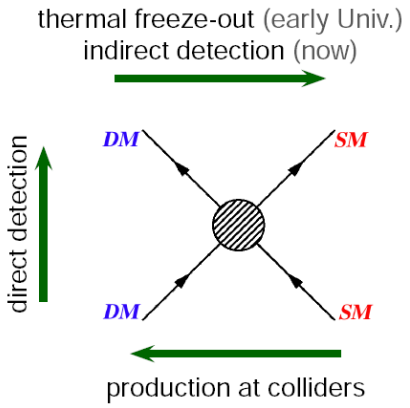

Figure 1.6: Three ways to detect DM particles interacting with baryonic particles. Credits: MPIK

1.5.1 Indirect Detectors

Indirect detectors search for gamma rays that come from the annihilation of two WIMPs in high DM density regions like galaxies. This search is practised by telescopes straightend towards these regions. But the detection of such gamma rays is not an evidence for DM yet because gamma rays are not completely understood by now. There are several gamma ray detectors in satellites like the Energetic Gamma Ray Experiment Telescope (EGRET) or the Gamma-ray Large Area Space Telescope (GLAST) [14].

1.5.2 Colliders

Colliders search for DM candidates by the collision of protons at very high energies. At the Large Hadron Collider (LHC) the lightest supersymmetrical particle could be observed by the missing transverse momentum in a collision [15]. For this observation two high-energy baryons are brought to a collision with a transverse momentum equal zero. Out of this collision different particles develop with non-zero transverse momenta which are summed up. When the total transverse momentum is non-zero that leads to particle that are not visible.

1.5.3 Direct Detectors

Direct detectors are run in underground laboratories. When WIMPs interact with nuclea three phenomena can be observed: Ionization, scintillization and phonons. Every direct detector looks for at least one of these phenomena, however, most detectors look for a combination of two. The most successful experiments to date are based on two different detector technologies. The first one is a cryogenic detector like Cryoneginc Dark Matter Search (CDMS) or Cryogenic Rare Event Search with Superconducting Thermometers (CRESST). Both collaboration use a germanium crystal detector operating at a temperature below 100 mK. They measures the phonons and the scintillation light of an interaction at the same time. The second detector technology uses noble gas detectors. In these detectors the target material is a noble gas such as xenon or argon. DarkSide is one example of a collabartion using argon as target material while the XENON collaboration uses xenon as target material. With noble gas detectors both scintillation light and ionization of the target material are used as signals.

2 The XENON Dark Matter Project

The XENON Dark Matter Project is an experiment to directly detect WIMPs by the recoil at a Xenon nucleus [16]. It is located in the Gran Sasso Underground Laboratory (LNGS) in Italy. This project is made up of three generations: XENON10, XENON100 and XENON1T, the latter is now starting. The detector used for this experiment is a double phase time projection chamber (TPC).

2.1 Principle of the TPC

The TPC is an invention of Dave Nygren in the late 1970s [17]. The TPC in the XENON project is built up as a two-phase TPC. This means it has a liquid xenon phase (LXe) and a gazeous xenon phase (GXe) on top. By the interaction between the WIMP and the nucleus two signals originate: A scintillation signal of the recoil and a scintillation signal of free electrons. The electrons are knocked out from Xe by the kinetic energy of the scattering particle. The signal of the recoil is generated directly, but the signal of the electrons arises from the drifting of the electrons from LXe to GXe. These signals are received by photomultiplier tubes (PMTs) fixed at the bottom and at the top of the TPC. Fig. 2.1 gives a schematic overview about the structure of a TPC.

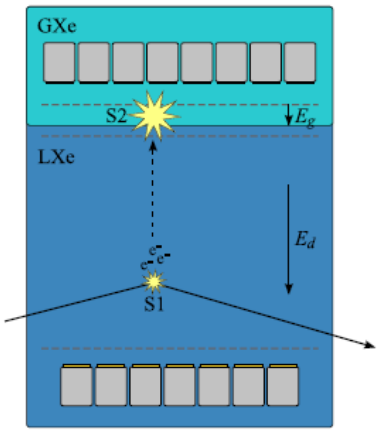

Figure 2.1: Measurement schema of a WIMP detection in a TPC. Figure from G. Plante

One advantage of the TPC is the possibility to determine the exact position of the interaction. X- and y-axis are located by the luminosity of every PMT itself and the z-position can be estimated by the time delay between S1 and

S2. Furthermore the comparison of S1 and S2 leads to a criterion of exclusion for the detected interaction. The ratio of the signals, S1/S2, is different for electron and nuclear events [18]. The set-up of the XENON100 detector is shown in fig. 2.2.

Figure 2.2: The XENON100 detector. Credits: XENON Dark Matter Project

2.2 Xenon as Detection Medium

Xenon (Xe) is a noble gas with an atomic weight of 131.293 g/mol. Its standard state is gazeous. The natural deposit of xenon is in the air, but it has only an extent of 0.087 ppm in the atomosphere. In standard pressure the boiling point of xenon is at 165.1 K and the melting point is at 161.4 K [19]. In fig. 2.3 a phase diagram of Xe in the range from -120 C to -80 C and from 0 bar to 4 bar is shown. The data points of the vapor pressure above the triple point are taken by [20]. The temperature of the vapor pressure below the triple point and the temperature of the liquid pressure is taken at which a densitiy of 22.59 mol/L is reached. The curves of the phase changes are fitted by MINUIT of ROOT with a χ^2-minimization. For the curve of the phase change of gaseous to liquid (black) the χ^2 is $\chi^2 = 0.0470588$ and the numbers of degrees of freedom are $NDf = 30$ lead to a fit of the form $p = \exp^{a \cdot T + b}$. The liquid to solid curve (red) with the form $p = a \cdot T + b$ leads to a $\chi^2 = 0.347078$ and $NDf = 30$. The gaseous to solid curve (green) has a $\chi^2 = 2.43673 \cdot 10^{-5}$ and $NDf = 1$ for a fit of the form $p = \exp^{a \cdot T + b}$. All of

these fits are just to illustrate the phase changes. To get better fit results I had to take more data points and add some error bars.

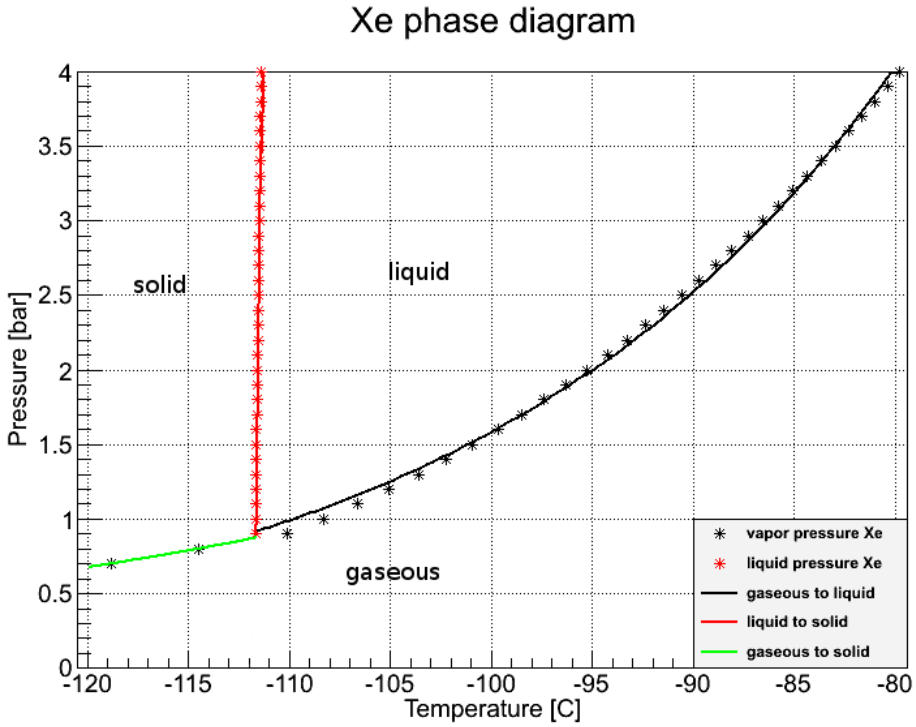

Figure 2.3: Phase diagram of Xe in the range from −120 C to −80 C and from 0 bar to 4 bar with the phase change of geseous to liquid (black), liquid to solid (red) and gaseous to solid (green).

Xenon has eight stable isotopes in nature, additional ^{136}Xe is with a half-life of $10^{21]}$ yr nearly stable [21]. For the DM research xenon is used because of the missing of any long-lived radioisotopes. The longest-live isotope ,^{127}Xe, has a half-live of 36.3 d. So the radioactive radiance of the target medium itself is nearly not existing. Furthermore xenon has two stable isotopes with non-zero nuclear spin ,^{129}Xe and ^{131}Xe, which can be used to try spin-dependent interaction with WIMPs.
The biggest advantadge of using LXe is the fiducialization of LXe. This means that LXe is self-shielding against background recoils. Another advantage of Xe is that the rate of WIMP detection is enhanced at low recoil energies due to the high atomic mass.
As mentioned in the subchapter before, the interaction of WIMPs with a xenon nucleus creates two scintillation signals. These two signals are in the vacuum ultraviolet range around 178 nm [22]. With a decay time of 2.2 (sin-

glet) and 27 (triplet) ns for the excited nucleus in an applied electric field, Xe is one of the fastest scintillators [23].

2.3 Installation at Gran Sasso

The LNGS is an underground laboratory for experiments in particle physics, particle astrophysics and nuclear astrophysics. The laboratory is placed on the side of a motorway tunnel crossing the Gran Sasso mountain. It shelters three experiment halls and service tunnel with a total volume of about 180,000 cubic meters. The cosmic ray flux is reduced by a factor of one million by the average 1400 m rock coverage and the neutrino flux is reduced by a thousend because of the smallness of Uranium and Thorium content in the dolomite rocks [24]. This makes it an ideal site to host low background experiments.

2.4 Results of XENON100

The second phase of the XENON Dark Matter Project is called XENON100. This phase started in 2008 with the installation at the LNGS and callibration measurements. The using of 100 kg Xe by 34 kg fiducial mass leads to a background reduction of 100 times. Between 2011 and 2012 there was a 224.6 days data run. Of this data run two events fell in the region of interest for WIMP search (fig. 2.4).

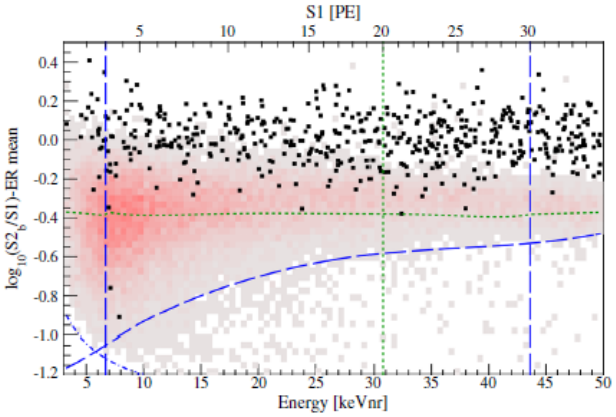

Figure 2.4: Logarithm of the ratio of recorded events substracted from the distribution's mean (black dots) in the space between 6.5 and 30.5 keVnr compared with a neutron callibration (red and grey). Fig. from Aprile et al., 2012

These events whose position is shown on fig. 2.5 are consistent with the total

background expectation of (1.0 ± 0.2) events [25] thus lead to a new limit on detector sensitivity rather than a discovery.

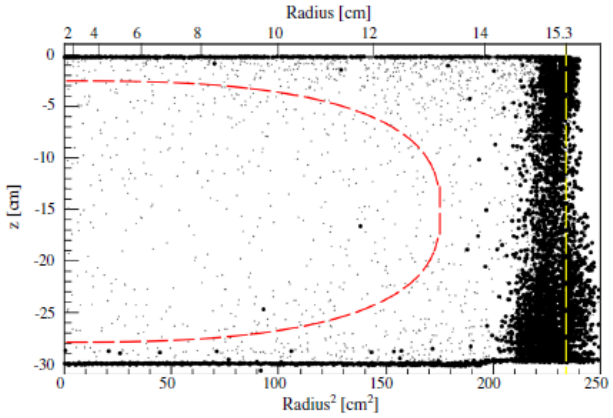

Figure 2.5: Location of recorded events with the expected ratio (black dots) and without (grey dots) inside the chamber (red line). Fig. from Aprile et al., 2012

The data sets of this experiment phase are added to a map of different experiments in fig. 2.6. The blue line is 90 % exclusion limit with the expected sensitivity shown by the green (1σ) and the yellow (2σ) band. As shown in this figure, the lower limits for the cross-section is decreased to 10^{-45} cm^2 by XENON100. The cross-section is the effective size of the nucleus that is "seen" by the WIMP. It is used as a scale of the probability that two particles interact with each other.

2.5 Status and Plans of XENON1T

2012 started the third generation of the XENON Dark Matter Project, the XENON1T experiment. At the time of this thesis, construction of the infrastructure buildings has begun. In difference to XENON100 the TPC will be filled with up to 2.6 T of LXe (fiducial mass is 1 T). This new generation should probe most of the WIMP parameter space predicted by theory by increasing the current experiment's sensitivity by two order of magnitude (fig. 2.7) [26].

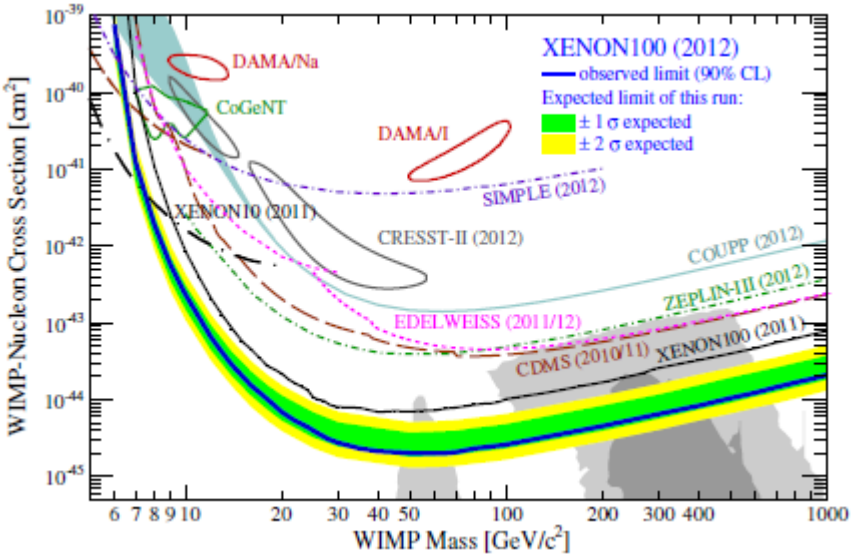

Figure 2.6: Result of XENON100 showing the exclusion limit (blue line) with 1σ (green) and 2σ (yellow) in comparison to other experiments and preferred regions (dark = 1σ, light = 2σ) for DM in supersymmetric models. Fig. from Aprile et al., 2012

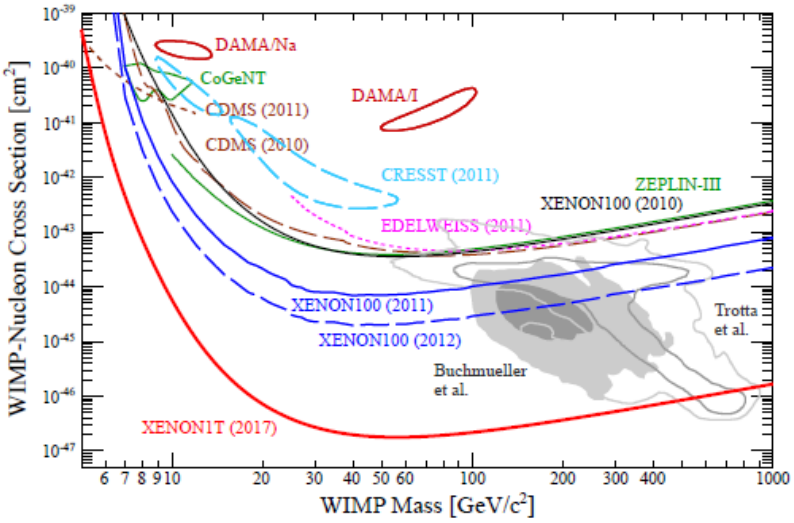

Figure 2.7: Projected limits of XENON1T (red) in comparison with the results from a selection of experiments and different regions predicted by different DM models. Fig. from Aprile et al.

3 Reflectivity Chamber in LXe

The reflectivity chamber (fig. 3.1) is an apparatus that measures the reflectivity of teflon (Polytetrafluoroethylene, PTFE). This measurement takes place in the environment of LXe. As light source is used a deuterium lamp that emits light with a wavelength of 178 nm corresponding to the scintillation light of LXe.

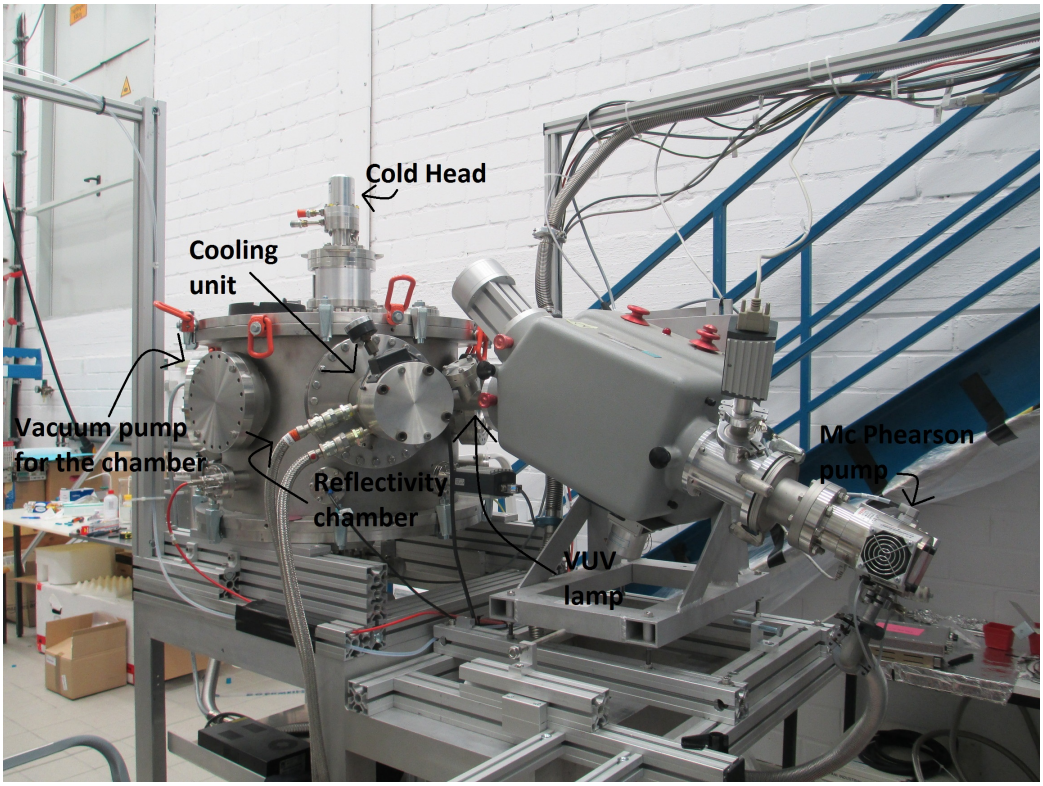

Figure 3.1: Reflectivity chamber. Fig from [27].

3.1 Motivation

Why do we want to investigate teflon? Teflon does reflect light of vacuum ultraviolet (VUV) wavelengths. Therefore it was used in XENON100 (fig. 3.2). Until now there were measurements of the reflectivity of PTFE in vacuum at LXe temperature [28]. But in fact we don't know enough about the reflectivity of teflon in LXe. Therefore the next measurements of the reflectivity of PTFE are placed in the direct environment of LXe.

Figure 3.2: The PTFE covering of the XENON100 detector. Credits: XENON Dark Matter Project

3.2 Installation

The two big components of the reflectivity chamber (fig. 3.1) are the main chamber where the reflection process happens and the VUV lamp. The VUV lamp is affiliated to a vacuum pump ("Mc Pherson" pump). Above the main chamber the cold head that cools down the LXe when it is conducted into the main chamber is placed. Another cooling unit is located on the side of the volume to cool down the photomultiplier (PMT). On the other side there is another vacuum pump only for the chamber. The inside of the reflectivity volume is shown in fig. 3.3. A black shield is installed around the collimator of the VUV lamp and the turnable PMT. It is an isolation shield for cooling down and heightening the vacuum in the main chamber. It is called black shield because it is black for the reason that it does not reflects the light beam. The black shield is also connected to the cooling unit.
In fig. 3.3 the quartz tube is missing. The glas tube is used to bring the PTFE in the environment of LXe in line with the light ray of the VUV lamp. The set-up for the measurement in shown in fig. 3.4.

3.3 Operating Principles

In the VUV lamp light with a wavelength of 178 nm is selected and focussed inside the chamber with the aid of a collimator. There the light ray encouters the glas tube with LXe and PTFE. On the PTFE the light ray is reflected. The PMT is driven by a motor around the glas tube and collects the reflected light beam. For the stabilisation of the PMT a waiting time of 5 sec is necessary before starting the measurement at each position. The glas tube with the PTFE can be turned and the angle of the PTFE can be read by a display onto the reflectivity chamber.

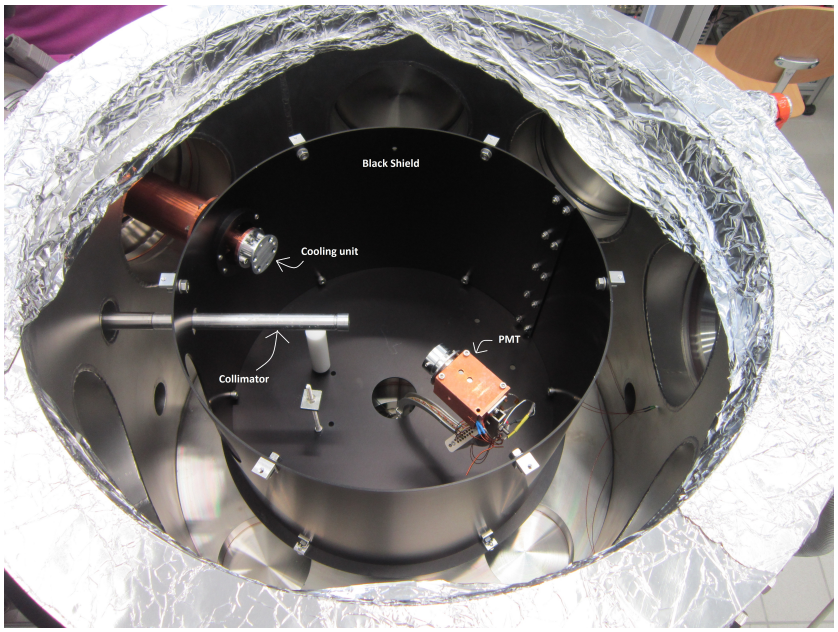

Figure 3.3: Look inside of the reflectivity chamber. Figure from [27]

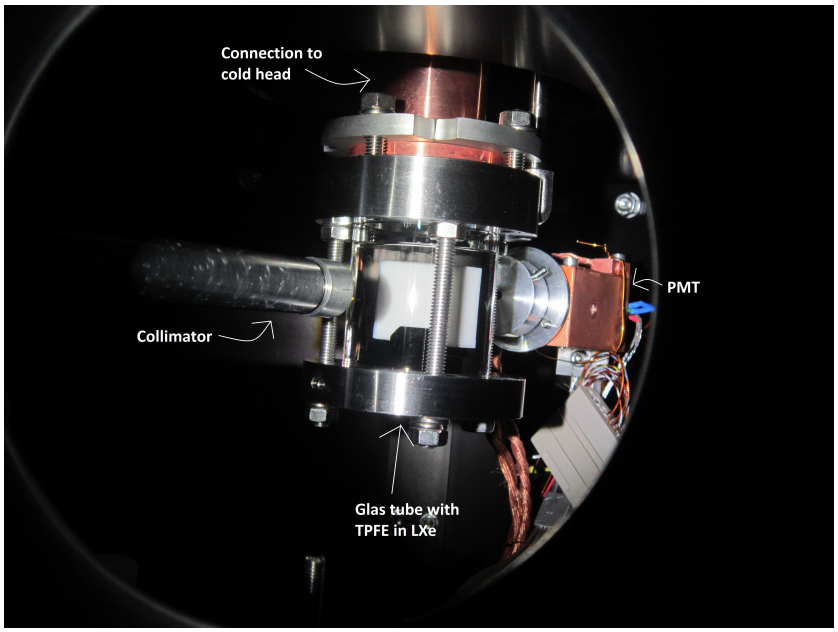

Figure 3.4: The collimator aimed at the glas tube filled with LXE and PTFE. The turnable PMT is behind the glas tube. Fig. from [27]

4 Slow Control

There are several things to monitor in the reflectivity chamber: The motor of the PMT, the pressure in the chamber and in the Mc Pherson pump and the temperature of the PMT and in the chamber. A slow control is a software allowing the monitoring of these parameters. In this chapter we take a look at the slow control for the pressure and temperature control.

4.1 Pressure and Temperature Control

The pressure and temperature control are programmed with LabVIEW. This is a programming system from National Instrument that is programmed with a visual programming language named "G" [29]. In LabVIEW there is a front panel (fig. 4.1) and a block panel (fig. 4.2). The front panel shows the temperature and the pressure in an absolute value and in a diagram. The block panel is the programming environment. The data is taken by the DAQ assistant that is connected to the reflectivity chamber. The temperature lines go in the "formulas" where the voltage that is given by the DAQ assistant which gets the voltages from PT100 sensors is converted into a temperature. Out of the tabular for temperature versus resistance for this type of temperature sensor [30] the temperature T at given voltage U is

$$T(U) = -241.1 + 2.271 \cdot \frac{U}{0.009} + 0.00132 \cdot \left(\frac{U}{0.009}\right)^2. \tag{4.1}$$

The pressure data p is calculated at the voltage U by

$$p(U) = 10^{\frac{U-7.75}{0.75}}. \tag{4.2}$$

This formula comes from the producer of the pumps [31].
Afterwards the data is displayed as absolute value and in the separate diagrams. Another string of each data is put together and is saved by the "Write to Measurement File" object. In the meantime there is a third temperature control for the temperature in the lab.
The pressure control is very important for the reflectivity chamber because the experiment is done in a high vacuum. High vacuum is needed because of particles that scatter the light ray when they are not eliminated and especially because of the water in the air which can condensate. In fig. 4.3 the vapor pressure curve of water is shown. The data and the fit are calculated by the approximated formula

$$p = 1.33322 \cdot \exp\left(20.386 - \frac{5132}{T/[\mathrm{C}] + 273.15}\right) \text{ mbar} \tag{4.3}$$

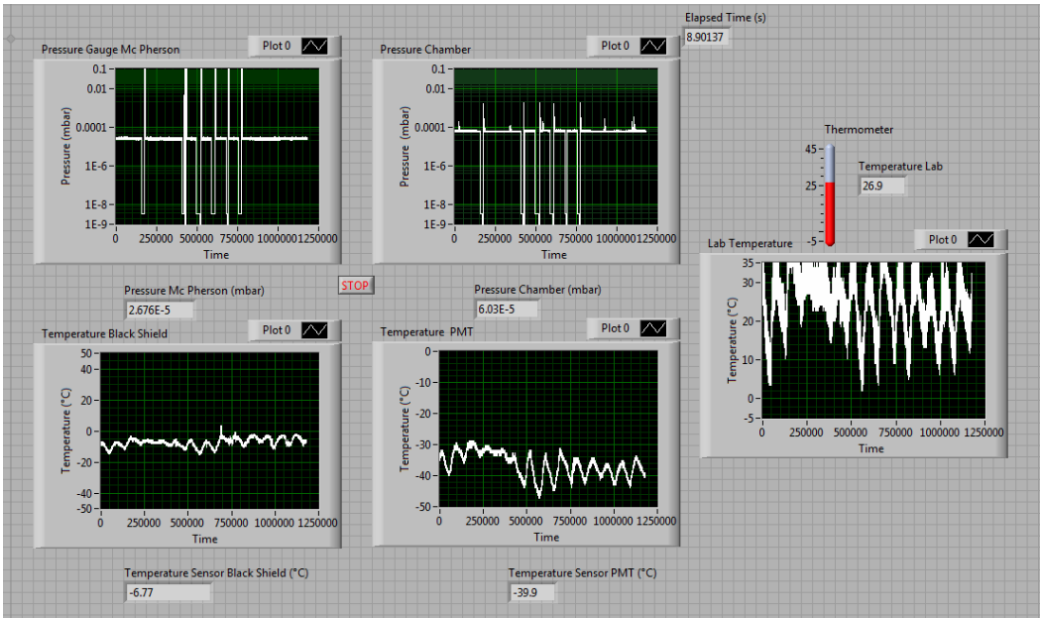

Figure 4.1: Front panel of the pressure and temperature control with two diagrams for the pressure and the absolute values plus three diagrams for the temperature and the absolute values at work. Together with [27]

that is based on the Clausius-Clapeyron relation

$$\frac{dp}{dT} = \frac{L}{T\Delta v} \tag{4.4}$$

with $\frac{dp}{dT}$ for the differential of the pressure p to the temperature T, the latent heat L and the specific volume change of the phase transition Δv [32].
At standard pressure water is solid at a temperature around -110 °C. This means for the reflectivity chamber, the water would condense and freeze on the glas tube that is cooled down by the LXe. But this ice would break the light beam. The vapor pressure of water at -110 °C is $2.1 \cdot 10^{-5}$ mbar. So the water is gaseous at a pressure of 10^{-5} mbar and a temperature of -110 °C. The vacuum pump can thus evacuate the chamber and the light beam can go directly through the glass tube.

4.2 Pressure Evolution at First Starting

The first starting of the vacuum pumps is shown in fig. 4.4. The black nearly constant data points are the pressure in the VUV lamp. This pressure is uncorrelated to the pressure in the chamber (red). The first drop (orange arrow) is from the backing pump that leads to a fore-vacuum wich is necessary

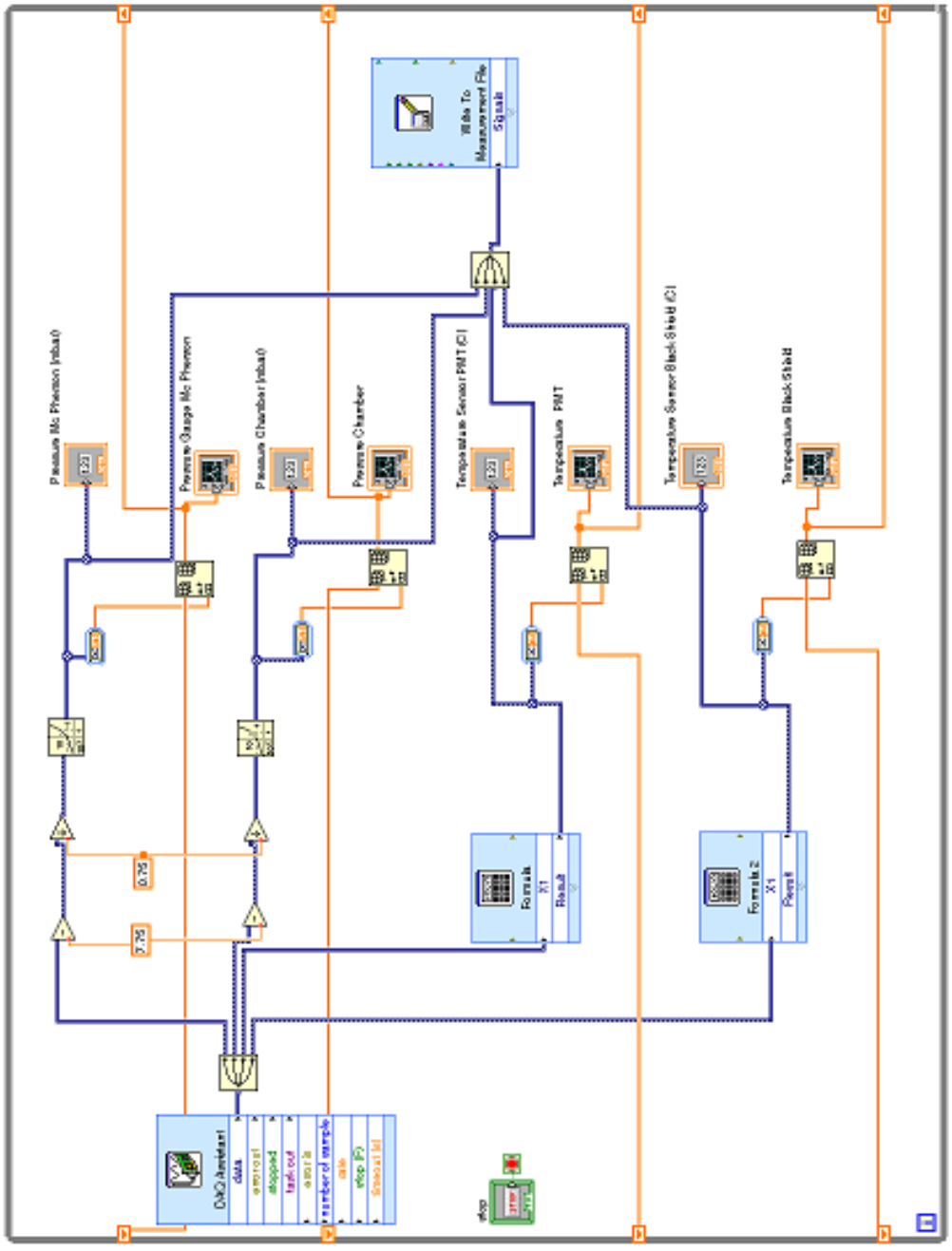

Figure 4.2: Block panel of the pressure and temperature control without the pressure control for the temperature in the lab. Together with [27]

before starting a turbo pump. The next drop (yellow arrow) is influenced by the high vacuum pump.
With this pump the pressure goes down to 10^{-6} mbar. This pressure is low enough to evaporate the condensation of the water at the glas tube. The last drop is influenced by the cold head (blue arrow). The next subchapter will focus on this. The area of the green arrow is remarkable. The kink that is seen could probably be a bigger impurity that is sucked out of the system.

4.3 Temperature Evolution in the Chamber

The temperature evolution in the time of the first starting of the vacuum pump for the chamber is fig. 4.5. The temperatures of the black shield (red) and of the PMT (black) have the same run. At the drop of the temperature the cold head is started (blue arrows). The cold head is nearer to the PMT than to the black shield. So the temperature of the PMT decreases more than the temperature of the black shield. It is visible that the last drop of the pressure (fig. 4.4) is at the same time like the cold head is started.
The correlation of the temperature in the chamber are also visible in fig. 4.6. This is another data set for three temperatures this time. The temperature at the PMT (black) and the temperature at the BS (red) like before supplemented with the temperature in the lab (green). It is observable that the run of the temperature in the lab is influencing the temperature in the chamber. That is the reason why it is important to keep the temperature of the lab nearly at the same level.

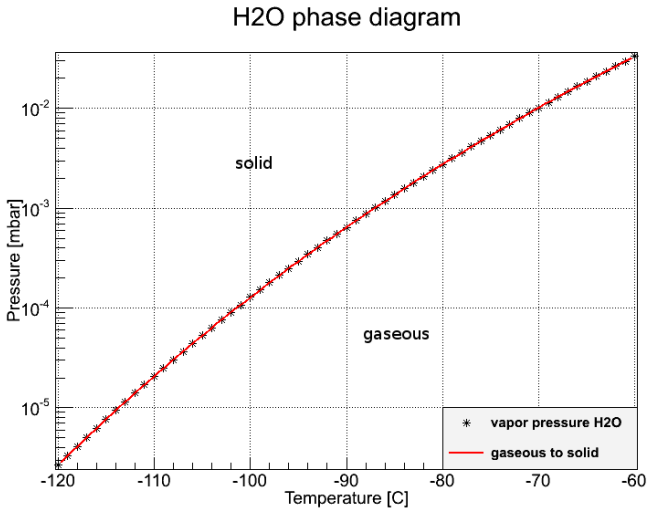

Figure 4.3: Vapor pressure curve of water at temperatures from -120 to -60 C and pressures from 10^{-6} to 10^{-1} mbar.

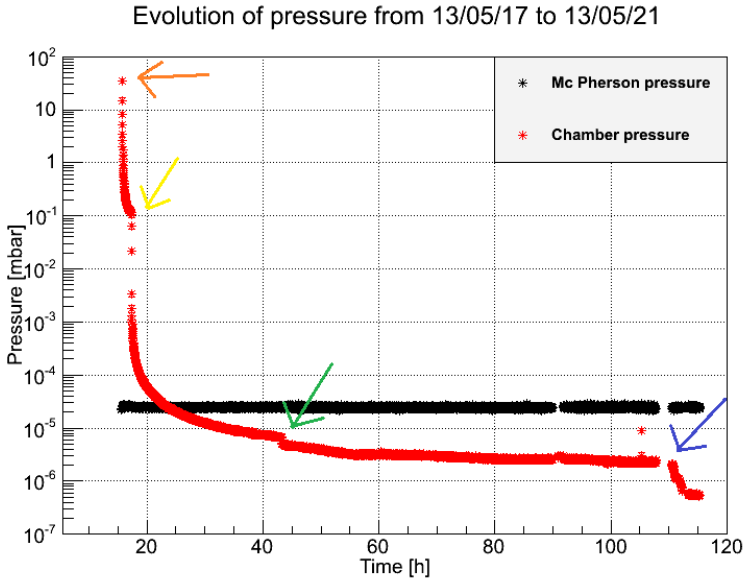

Figure 4.4: The pressure evolution by the first time starting vacuum pump in the chamber (red) and by the Mc Pherson pump (black) at the same time. The starting of the backing pump (orange arrow), the starting of the high vacuum pump (yellow arrow), the sucking out of a big impurity (green arrow) and the starting of the cold head (blue arrow) are drawn in.

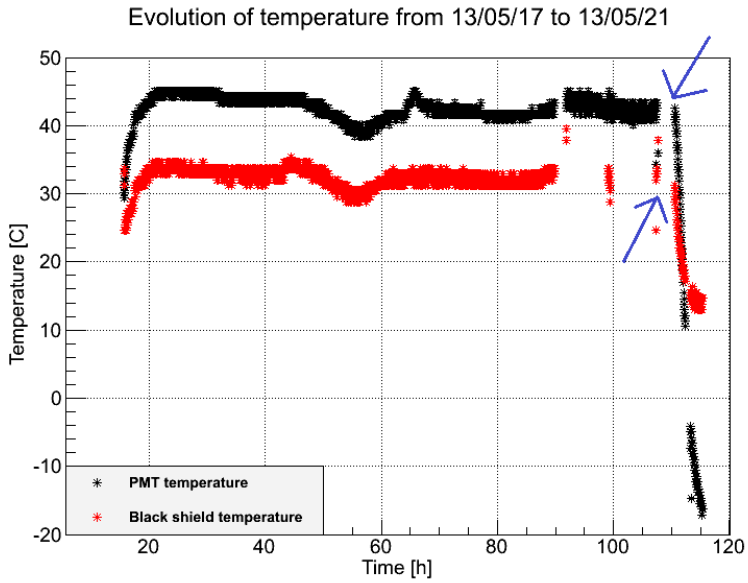

Figure 4.5: Evolution of the temperature at the PMT and at the black shield at the time of the first starting of the vacuum in the chamber. The blue arrows show where the cold head is started.

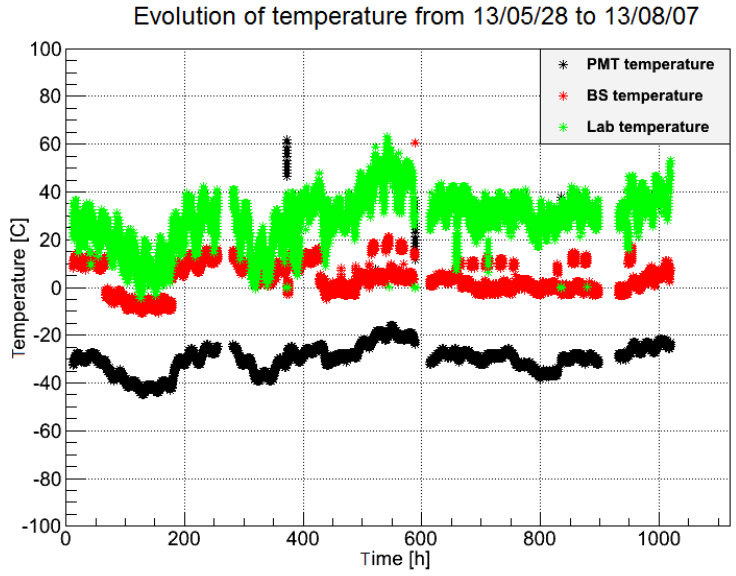

Figure 4.6: The evolution of temperature in the lab (green), at the PMT (black) and at the BS (red) from the 28th of May to the 8th of July.

5 PMT Characterization

The reflectivity of the PTFE is scanned by a turnable PMT that is shown in fig. 5.1. This PMT has to run with its best power. Therefore the changeable parameters of the PMT need to be tested. These parameters are the high voltage (HV) that is affiliated to the PMT and the discrimination value of the trigger logic.

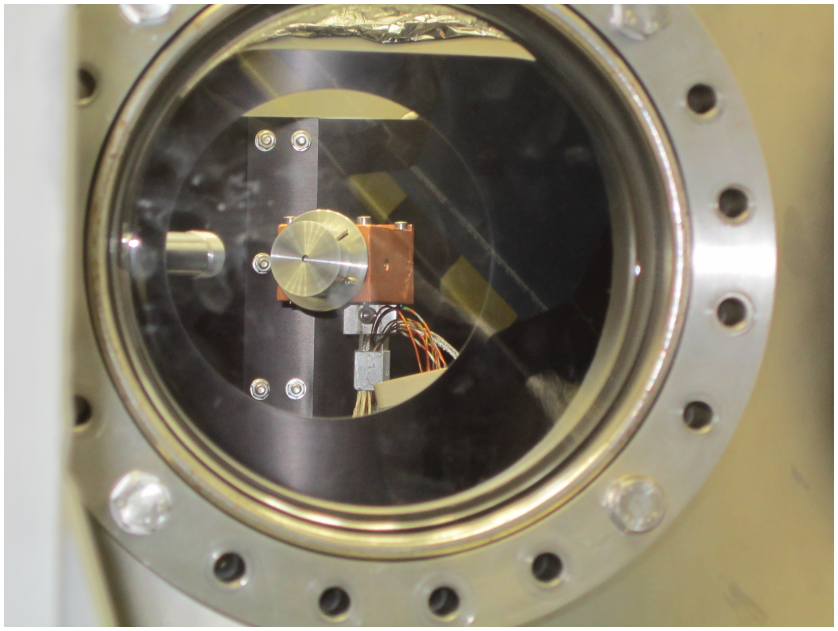

Figure 5.1: Look at the turnable PMT through a window of the reflectivity chamber. Fig. from [27]

5.1 PMT and Trigger Logic

The schematic logic of a PMT is shown in fig. 5.2. A photon comes in and knocks an electron out of a photocathode by the external electric effect [33]. This electron is accelerated to a dynode where it knocks out some other electrons that are accelerated to another dynode where those knock out some electrons and so on thus provocing a cascade of electrons. This process stops at an anode.
At this anode a HV is applied. The arriving electrons cause a short negative pulse in this voltage that can be measured by a leading edge discriminator (LED, as the one shown in fig. 5.3) trigger. The trigger records the negative pulses, inverts them and digitizes them automatically. This process is shown in fig. 5.4.

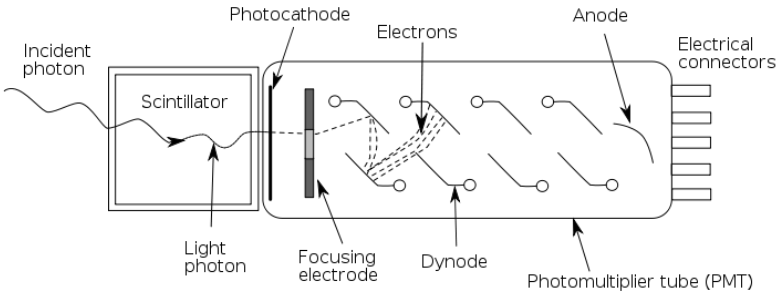

Figure 5.2: Schematic structure of a PMT. The photon encounters the photocathode and knocks out an electron. That electron is accelerated to a dynode where itself knocks out photons. These photons are themself accelerated to another dynode. This process goes further till the photons come to an anode at which a high voltage is applied. Fig. from C. Eberhardt

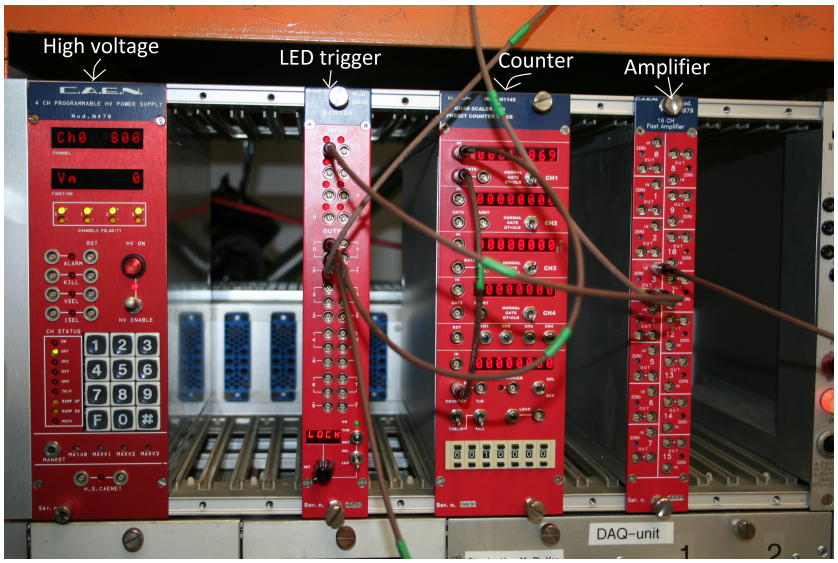

Figure 5.3: The LED trigger used for the reflectivity chamber with the HV display, the amplifier and the counter. Fig. from [27]

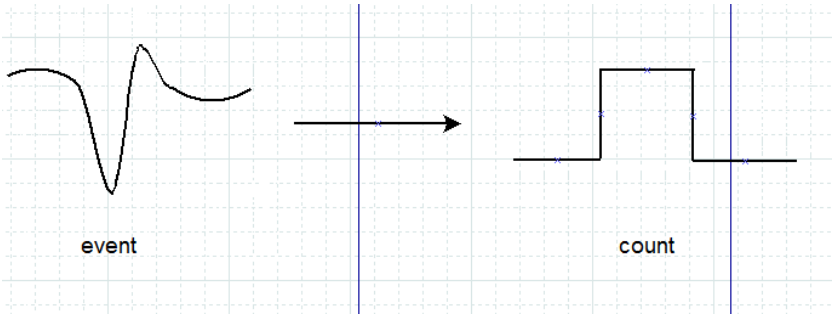

Figure 5.4: Logic of the LED trigger. The negative pulse with a certain height are recorded, inverted and digitized by the LED trigger.

5.2 Stabilisation of the PMT

To get the best parameters for the PMT it has to be stabe when shone with light from the lamp. So it is necessary to check the PMT on its stability. This is made by starting the VUV lamp and the PMT and recording the counts as time process (fig. 5.5). The count rate is increasing up to 110 min. The heights occuring later and later for 10 min are eye-catching. Where the heights come from is unknown but those do not influence the measurement as we will see afterwards. After 110 min the heights also happen at big enough time interval that they do not hinder data taking. Because of the stability after 110 min the measurements were started after 120 min of stabilisation.

5.3 Characterization at 100 mV

The first characterization of the PMT was made with a discrimnation value of 100 mV for the trigger. Therefore data with the lamp on and with the lamp off was taken. Data with the lamp off are the background counts. The HV on the PMT was changed by 5 V. Out of the data the ratio of counts with lamp on and background

$$\text{Ratio} = \frac{\text{Counts with lamp on}}{\text{Background counts}} \tag{5.1}$$

was calculated. The ratio of counts with lamp on and background is used because it leads to the best resolution of counts for the PMT. Because it was taken the ratio the heights of fig. 5.5 don't influence the measurements. The ratio for a discrimination value of 100 mV is outlined in fig. 5.6.
The error bars of the ratio are taken by the Gaussian error propagation with

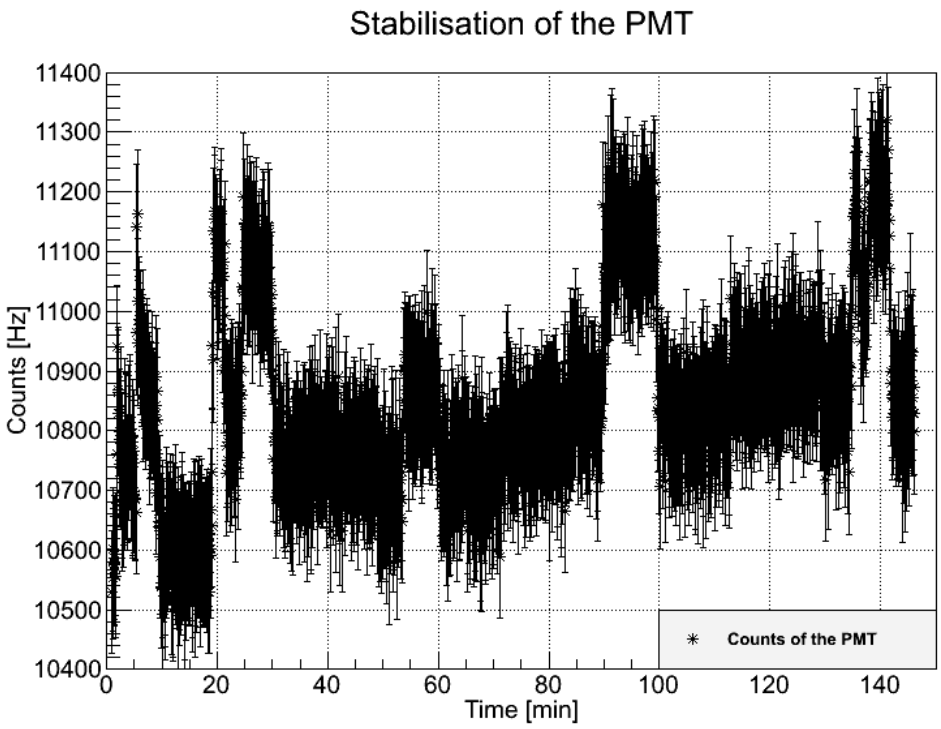

Figure 5.5: Count data after starting the PMT and the VUV lamp.

an assumed error of $\sqrt{n}$:

$$
\begin{aligned}
y &= \frac{x_1}{x_2} \\
\Delta y &= \sqrt{\left(\frac{\partial y}{\partial x_1}\Delta x_1\right)^2 + \left(\frac{\partial y}{\partial x_2}\Delta x_2\right)^2} \\
\Delta y &= \sqrt{\left(\frac{Deltax_1}{x_2}\right)^2 + \left(\frac{-x_1 \cdot \Delta x_2}{x_2^2}\right)^2} \\
\Delta y &= \sqrt{\left(\frac{\sqrt{x_1}}{x_2}\right)^2 + \left(\frac{-x_1\sqrt{x_2}}{x_2^2}\right)^2} \\
\Delta y &= \sqrt{\left(\frac{x_1}{x_2^2}\right) + \left(\frac{x_1^2 \cdot x_2}{x_2^4}\right)} \\
\Delta y &= \sqrt{\left(\frac{y}{x_2}\right) + \left(\frac{y^2}{x_2}\right)}. \qquad (5.2)
\end{aligned}
$$

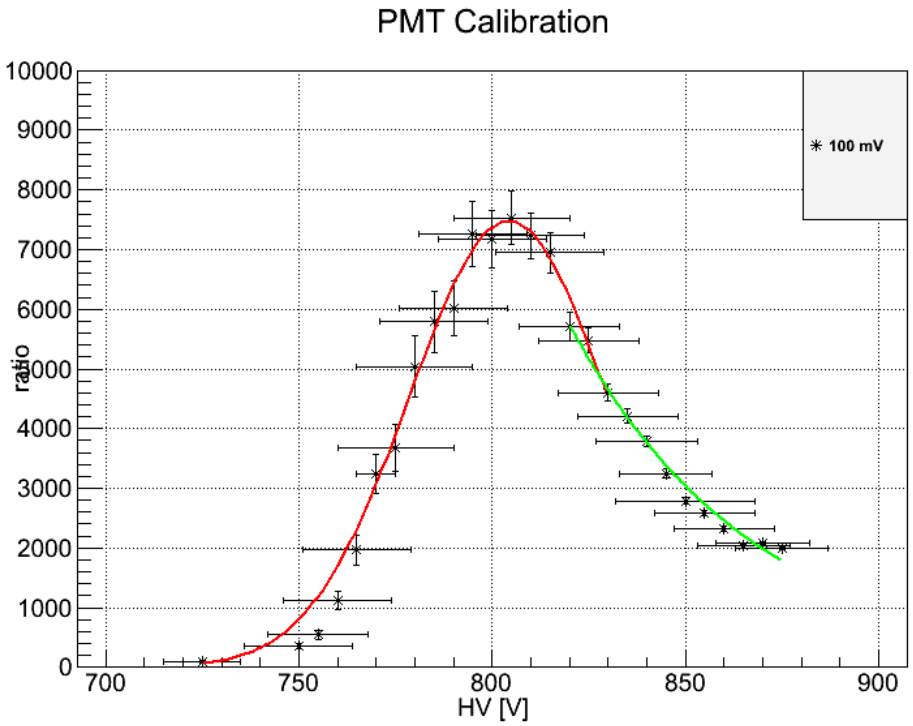

Figure 5.6: The ratio of counts with lamp on to background counts versus the applied HV on the PMT for a discrimination value of 100 mV. The error bars of the HV are taken by the difference that the HV display reports to the HV that was set. The error bars of the ratio are from the Gaussian error propagation with the square-root of the counts and the square-root of the background counts. The data is approximated with a Gaussian fit (red) and an exponential fit (green)

The error bars of the HV are the absolute value of the difference between the HV that was set and the HV that was displayed:

$$\Delta\text{HV} = |\text{HV}_{\{textset} - \text{HV}_{\text{displayed}}|. \tag{5.3}$$

The approximated fits are a Gaussian distribution (red) and an exponential fit (green). The values of the Gaussian distribution are in table 5.1, the values of the exponential fit are in table 5.2.
For the Gaussian fit there is $\chi^2 = 1.11$ and $NDf = 15$. This leads to a reduced χ^2 $\chi^2_{\text{red}} = \frac{\chi^2}{NDf}$ of $\chi^2_{\text{red}} = 0.074$. The exponential fit has $\chi^2 = 0.55$ and $NDf = 10$ and $\chi^2_{\text{red}} = 0.055$. These reduced χ^2s are very low. That means the fits are too good. The reasons are the big errors of the HV and the chosen borders of the fits.

5.4 Characterization at Different Trigger Values

In the same way like for the discrimation value of 100 mV the counts with lamp on and the background counts were taken at different discrimination values. The adjusted discrimination values are 10 mV, 50 mV, 75 mV, 100 mV and 125 mV. Again the ratio was calculated by 5.1. For this different discrimation values the HV was changed by 25 V. The ratio versus the HV for different discrimination values is shown in fig. 5.7.
The values of the fit parameters for the Gaussian fit for the different discrimination values are given in table 5.3.
The values of the Gaussian fit for the discrimination value of 10 mV have an error that is too big. This is because there were used just two data points for fitting the Gaussian distribution. This will be also seen in the χ^2 and the NDf. The values of 100 mV discrimination value are consistent in the error with the values that were found out in fig. 5.6.
The χ^2, the NDf and the χ^2_{red} of the Gaussian fits are given in table 5.4.
The only χ^2_{red} that is near to 1 is from the discrimination value of 125 mV. This leads to the assumption that for better fits there are too little points. But these fits are only an approximation of the data points to get an idea of what discrimination value does one get the biggest maximum which is the mean of every Gaussian fit. With better fits the errors of the parameters could be smaller.
The values for the exponential fits for different discrimination values are given in table 5.5.
The χ^2, the NDf and the χ^2_{red} of the exponential fits are given in table 5.6.
Again it is obvious that the χ^2_{red} are too small. This is also because there are too little data points. But just to get an ideo of the progress of the data

Parameter	Value
Constant	(7474 ± 353)
Mean	(804 ± 4)
Sigma	(26 ± 3)

Table 5.1: Values of the parameters for the Gaussian fit (red in fig. 5.6)

Parameter	Value
Constant	(26 ± 3)
Slope	(-0.021 ± 0.004)

Table 5.2: Values of the parameters for the exponential fit (green in fig. 5.6)

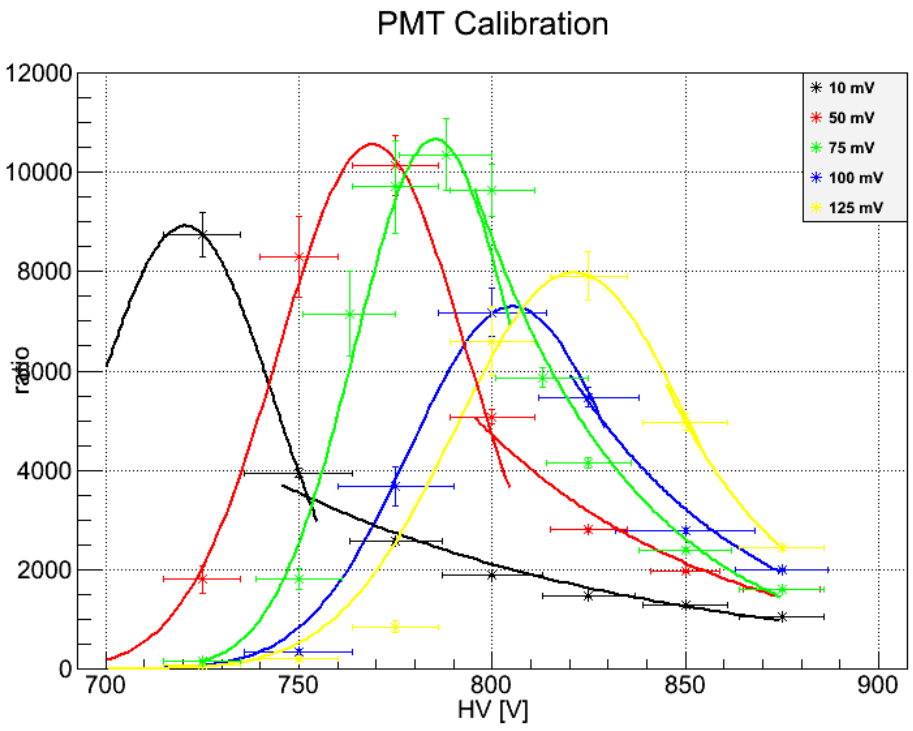

Figure 5.7: The ratio of counts with lamp on to background counts versus the applied HV on the PMT for different discrimination values (10 mV, 50 mV, 75 mV, 100 mV and 125 mV). The error bars of both values are taken like in fig. 5.6. Each data set is approximated with a Gaussian fit and an exponential fit

Disc. value	Constant	Mean	Sigma
10 mV	(8915 ± 9204)	(720 ± 141)	(23 ± 96)
50 mV	(1056 ± 155)	(769 ± 7)	(24 ± 6)
75 mV	(1066 ± 145)	(785 ± 9)	(21 ± 6)
100 mV	(7297 ± 883)	(805 ± 9)	(27 ± 4)
125 mV	(7981 ± 624)	(821 ± 8)	(31 ± 4)

Table 5.3: Values of the parameters for the Gaussian fits for different discrimination values (red in fig. 5.7)

Disc. value	χ^2	NDf	χ^2_{red}
10 mV	$2.9 \cdot 10^{-9}$	0	n.d.
50 mV	0.09	1	0.09
75 mV	0.42	3	0.14
100 mV	0.31	2	0.155
125 mV	2.56	3	0.853

Table 5.4: Values of the parameters for the Gaussian fits for different discrimination values (red in fig. 5.7)

Disc. value	Constant	Slope
10 mV	(16 ± 1)	(-0.010 ± 0.002)
50 mV	(21 ± 3)	(-0.016 ± 0.003)
75 mV	(28 ± 3)	(-0.024 ± 0.004)
100 mV	(24 ± 5)	(-0.020 ± 0.006)
125 mV	(33 ± 8)	(-0.029 ± 0.009)

Table 5.5: Values of the parameters for the exponential fits for different discrimination values (red in fig. 5.7)

Disc. value	χ^2	NDf	χ^2_{red}
10 mV	2.63	4	0.6575
50 mV	1.47	2	0.735
75 mV	0.73	3	0.243
100 mV	0.16	1	0.16
125 mV	$2.9 \cdot 10^{-8}$	0	n.d.

Table 5.6: Values of the parameters for the exponential fits for different discrimination values (red in fig. 5.7)

points the approximations are good enough.
Out of fig. 5.7 the best parameters for the PMT that means the highest ratio is reached, are a discrimation value of 75 mV and a HV of (785 ± 9) V.

5.5 Trigger efficiency

It is also important to know for the measurement of the reflection how many counts are seen by the LED trigger and how much is overlooked. Therefore it was taken with an oscilloscope the rate of signals and the rate of counts. Out of this data the trigger efficiency was calculated by

$$\text{Trigger efficiency} = E_T = \frac{\text{Rate of counts}}{\text{Rate of signals}} = \frac{R_C}{R_S}. \tag{5.4}$$

The errors of the HV are again 5.3. The errors of the trigger efficiency are

$$\Delta T_E = \sqrt{\left(\frac{\Delta R_C}{R_S}\right)^2 + \left(\frac{-R_C \cdot \Delta R_S}{R_S^2}\right)^2} \tag{5.5}$$

whereat ΔRate of counts and ΔRate of signlas the fluctuations around the taken values are, given by the oscilloscope. The trigger efficiency for a discrimation value of 75 mV versus different HVs is shown in fig. 5.8.
Around the HV of (785 ± 9) V the trigger efficiency has a value around 90 %. This value is good enough to measure the reflectiviy of PTFE with these parameters for the PMT. Consequently the instruments are adjusted to a trigger threshold of 75 mV and the data should always be taken at 785 V.

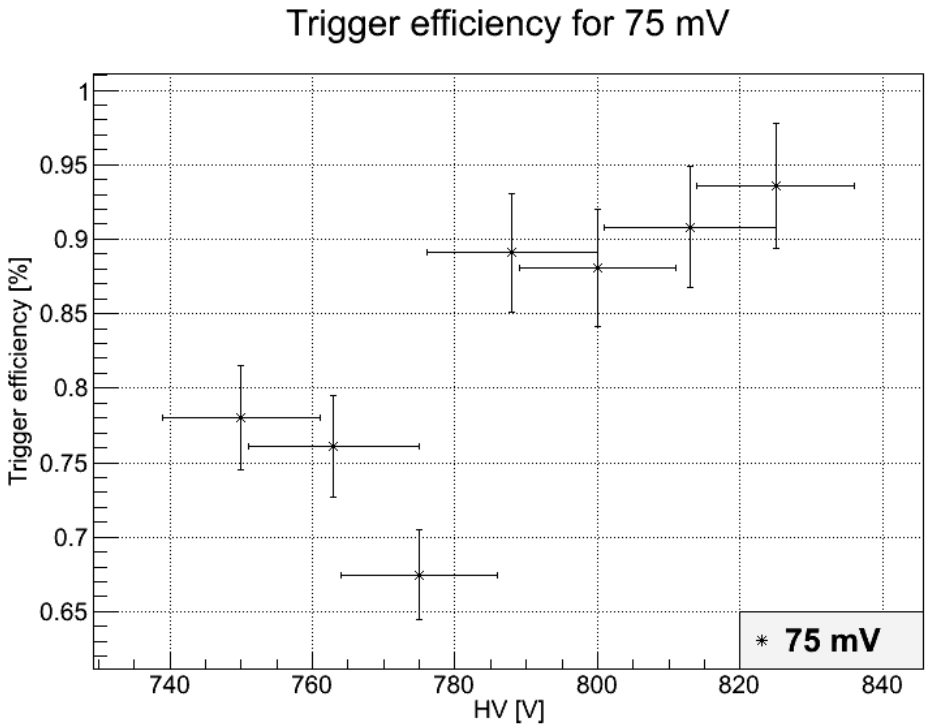

Figure 5.8: The efficiency of the LED trigger for the discrimination value of 75 mV versus HV.

6 Conclusion

This thesis was about the set-up and test of the slow control and the characterization of the PMT.
For the set-up of the slow control I worked with LabVIEW and learned how to use it for data taking with LabVIEW, direct data storage and simultanious visualization of the data on a display.
But the slow control is only needed when the apparatus to measure is already built up. So I helped to build it directly in the laboratory. First of all I learned how to behave in a lab. Furthermore I learned a lot about cleaning the components for the apparatus. Last but not least I learned a lot about the design of a physical measurement system. By taking data of this system I got to know the important components of a physical measurement like the LED trigger.
The data taken by the slow control and by myself needed to be analysed. At this point I learned more about data analysing with ROOT. In a playful way I began with the phase diagram of xenon and water. Here I got to know with internet data base for physical properties of elements ([20]) or approximation formulars (as 4.3). The next step was to visualize my own data sets. This is made for the pressure and temperature control where a correlation between the temperatures can be seen and no correlation between the pressures. That the pressures do not correlate is very important for the set-up of the measurement because it means that both parts of th system are independent from each other. Furthermore the required pressure is reached in the chamber that the water does not condensate at the glass tube.
Finally I learned how to fit with MINUIT in ROOT. By this step I found out that best values for the PMT that is used in this apparatus are a discrimination value of 75 mV and a HV of (785 ± 9) V with a trigger efficiency of 90 %.
By writing these thesis I want to make my results available to the public. By this step I learned about the connection between the theory and the experimental parts of physics.
These four components were just the obvious parts of my work. The work in the XENON collaboration of the university of Muenster is an invaluable experience for my way to pursue a physical career.

References

[1] A. Einstein: Kosmologische Betrachtungen zur allgemeine Relaetivitatstheorie. Sitzungsbericht der Preussischen Akademie der Wissenschaften zu Berlin, 142-152 (1917)

[2] G. Lemaitre: Expansion of the universe, A homogeneous universe of constant mass and increasing radius accounting for the radial velocitiy of extra-galactic nebulae. Monthly Notices of the Royal Astronomical Society, 91, 483-490 (1931)

[3] F. Zwicky: Spectral Displacement of Extra Galactic Nebulae. Helv. Phys. Acta, 6 (1933), 110.

[4] S. Garbari et al.: Limits on the local dark matter density. arXiv:1105.6339v2 (2011)

[5] A. Einstein: Die Grundlagen der allgemeinen Relativitatstheorie. Annalen der Physik, 49, 769-882 (1916)

[6] E. Hubble: A relation between distance and radial velocity among extra-galactic nebulae. Proc. N.A.S., 15, 168-173 (1929)

[7] P. H. Dicke et al.: Cosmic Blac-Body Radiation. Astrophysical journal, 142, 414-419 (1965)

[8] A. A. Penzias & R. W. Wilson: A Measurement of Excess Antenna Temperature at 4080 Mc/s. Astrophysical journal, 142, 419-421 (1965)

[9] CERN 2013: The Early Universe. home.web.cern.ch/about/physics/early-universe (2013/08/01)

[10] J. Dunkley et al.: Five-Year Wilkinson Microwave Anisotropy Probe (WMAP) Observations: Bayesian Estimation of CMB Polarization Maps. arXiv:0811.4280v2 (2009)

[11] H. Murayama: Supersymeetry Phenomenology. arXiv:hep-ph/00022232v2 (2013)

[12] J. W. F. Valle: Neutrino mass in supersymmetry. arXiv:0911.3103 (2009)

[13] A. Einstein: Ist die Traegheit eines Koerpers von seinem Energiegehalt abhaengig? Annalen der Physik, 323, 639-643 (1905)

[14] M. Cirelli: Indirect Searches for Dark Matter: a status review. arXiv:1202.1454v5 (2013)

[15] I. Hinchliffe et al.: Precesion SUSY Measurement at LHC. arXiv:hep-ph/9610544 (1996)

[16] E. Aprile et al.: Simultaneous Measurement of Ionization and Scinillation from Nuclear Recoils in Liquid Xenon for a Dark Matter Experiment. Physical review letters, 97 (2006)

[17] S. Klein: The time projection chamber turns 25. cern-courier.com/cws/article/cern/29014 (2013/08/05)

[18] M. Schumann: The XENON Detector. xenon.physics.rice,edu/detector/html (2013/08/05)

[19] M. Winter: Xenon: the essentials. www.webelements.com/xenon/ (2013/08/06)

[20] http://webbook.nist.gov/chemistry/fluid/ (2013/08/19)

[21] N. Ackerman et al.: Observation of Two-Neutrino Double-Beta Decay in 136Xe with EXO-200. arXiv:1108.4193 (2011)

[22] J. Jortner et al.: Localized Excitations in Condensed Ne, Ar, Kr, and Xe. J. Chem. Phys., 42, 4250 (1965)

[23] S. Kubota et al.: Evidence for a triplet state of the self-trapped exciton states in liquid argon, krypton and xenon. J. Phys. C, 11, 2645 (1978)

[24] R. Antolini: LNGS - Gran Sasso National Laboratory. www.lngs.infn.it/lngs_infn/ (2013/08/06)

[25] E. Aprile et al.: Dark Matter Results from 225 Live Days of XENON100 Data. Physical review letters, 109, 181301 (2012)

[26] E. Aprile et al.: The XENON1T Dark Matter Search Experiment. arXiv:1206.6288v1 (2012)

[27] C. Levy-Brown: Upcoming PhD thesis. (2014)

[28] B. Choi: The Light Response of the XENON100 Time Projection Chamber and the Measurements of the Optical Parameters with the Xenon Scintillation Light. (2013)

[29] National Instruments Corporation: LabVIEW System Design Software. www.ni.com/labview/ (2013/08/20)

[30] Thermocouple Instruments Limited: PT100 Resistance Table. www.micropik.com/PDF/pt100.pdf (2013/08/28)

[31] Oerlikon Leybold Vacuum GmbH: Ionivac ITR 90/ITR 90 P - Instruction Sheet. www.idealvac.com/files/manuals/Leybold-ITR90-Gauge-Specs-Data-Sheet01.pdf (2013/08/28)

[32] W. R. Salzman: Clapeyron and Clausius-Clapeyron Equations. www.chem.arizona.edu/ salzmanr/480a/480ants/clapeyro/clapeyro.html (2013/08/20)

[33] A. Einstein: Ueber einen die Erzeugung und Verwandlung des Lichts betreffenden heuristischen Gesichtspunkt. Annalen der Physik, 17, 132-148 (1905)